https://doi.org/10.5194/gmd-2024-189
Preprint. Discussion started: 30 April 2025

Geoscientific Model Development
Discussions

Adjoint-Based Simultaneous State and Parameter Estimation in an Arctic Sea Ice-Ocean Model using MITgcm (c63m)

Guokun Lyu[1,2], Longjiang Mu[3], Armin Koehl[4], Ruibo Lei[1*], Xi Liang[5], and Chuanyu Liu[6]

[1]Key Laboratory for Polar Science, Polar Research Institute of China, Ministry of Natural Resources, Shanghai, 200136, China
[2]Shanghai Key Laboratory of Polar Life and Environment Sciences, School of Oceanography, Shanghai Jiao Tong University, Shanghai, 200230, China
[3]Laoshan Laboratory, Qingdao, 266100, China
[4]Center for Earth System Research and Sustainability (CEN), Universität Hamburg, Hamburg, 54662, Germany
[5]Key Laboratory of Marine Hazards Forecasting, National Marine Environmental Forecasting Center, Ministry of Natural Resources, Beijing, 100081,China
[6]Key Laboratory of Ocean Observation and Forecasting, and Key Laboratory of Ocean Circulation and Waves, Institute of Oceanology, Chinese Academy of Sciences, Qingdao, 266000, China

Corresponding to: Ruibo Lei (leiruibo@pric.org.cn)

Abstract. Parameters in sea ice-ocean coupled models greatly affect the simulated ocean and sea ice evolution, and are normally tunned to bring the model state close to the observations. Using an adjoint method, spatiotemporally varying parameters of Arctic sea ice-ocean coupled model are optimized simultaneously with the initial condition and the atmospheric forcing by assimilating satellite and in-situ observations. The assimilation results show that the joint state and parameter estimation (SPE) substantially improves the sea ice concentration simulation. Particularly in October when the ocean surface starts to refreeze, SPE reduces the lead closing parameter H_o, which determines the minimum ice thickness formed in the open water, to increase the lateral sea ice growth and facilitate the seasonal rapid sea ice recovery in the Pacific sector. Comparisons with sea ice thickness observations from the moored upward looking sonars and Ice Mass Balance buoys demonstrate that the inclusion of model parameters in the optimization also leads to better sea ice thickness estimation. Overall, the adjoint-based SPE scheme has the potential to better reproduce the Arctic ocean and sea ice state and will be applied to reproduce a new Arctic sea ice-ocean reanalysis.

https://doi.org/10.5194/gmd-2024-189
Preprint. Discussion started: 30 April 2025

1 Introduction

In climate models, parameterizations are widely used to simulate the effects of unresolved processes on the large-scale state variables. The parameters in the parameterizations affect the model simulations largely at various spatial and temporal scales (e.g., Mauritsen et al., 2012; Murphy et al., 2004), and they are particularly important for the Arctic system, where observations are extremely scarce and key processes are undergoing rapid changes.

Most of the model parameters cannot be measured straightforwardly. Usually, a globally uniform value for individual parameters are assumed as default in the parameterization schemes. When incorporated into complex climate models, the sensitive parameters are further adjusted to bring the model's climatology close to the observed state (e.g., Hourdin et al., 2017; Mauritsen et al., 2012). The underlying assumption is that these sensitive parameters determine the model's climatology. Over the past decades, manually (e.g. Mauritsen et al., 2012) and automatic tunning (e.g., Jackson et al., 2008; Williamson et al., 2013; Yang et al., 2013) methods have been developed to optimize a number of sensitive parameters (order of 10). In addition, data assimilation techniques, including the ensemble Kalman Filter (Annan et al., 2005; Massonnet et al., 2014; Wu et al., 2012) and the adjoint method (Liu et al., 2012; Lyu et al., 2018), are also tested for the spatiotemporal-varying parameters with huge dimensions.

In the sea ice models, parameters also greatly affect the sea ice seasonal and interanual evolutions and the heat, freshwater and momentum budget of the sea ice-ocean-atmosphere system (e.g., Kim et al., 2006; Uotila et al., 2012). Similar to climate models, these parameters are tuned manually through a trial and error process to match the historical sea ice state (e.g., Hibler, 1979; Miller et al., 2005). Automated parameter estimation methods, such as genetic algorithms (Sumata et al., 2019), ensemble Kalman filters (Massonnet et al., 2014), and the adjoint method (Lu et al., 2021; Lyu et al., 2018; Panteleev et al., 2020), are applied to optimize sensitivite parameters using satellite sea ice observations. More recently, machine learning (e.g., Bretherton et al., 2022; Horvat & Roach, 2022; Kochkov et al., 2024) has been applied to develop the sub-grid parameterization using high-resolution model simulations and reanalysis datasets. However, the overall improvements on the observed variables usually come with detrimental effects on the other variables or at some regions. For instance, Massonnet et al. (2014) reported that the improvements on sea ice speed come with an overestimation of winter ice areal outflow through the Fram Strait.

Several causes are likely responsible for these detrimental effects. Firstly, the model parameters are only parts of the model uncertain inputs, and these parameters may get over-adjusted to compensate for errors in the other model uncertain inputs. For instance, Miller et al. (2005) suggested that the optimal parameters likely compensate for the deficiencies in the atmosphere forcing. Therefore, it is necessary to optimize the model uncertain inputs simultaneously. Secondly, the sensitivities of the sea ice state to parameter perturbations show clear spatiotemporal patterns (Kim et al., 2006; Miller et al., 2005), suggesting that allowing the optimized parameters to vary geographically and temporally is likely further improve the model performance. Additional, it is necessary to use more comprensive Arctic ocean and sea ice observations to constrain the model parameters and the other uncertain inputs.

In the framework of data assimilation, simultaneous state and parameters estimation (SPE) can be realized by including the spatiotemporally varying parameters in the set of control variables (e.g., Hu et al., 2010; Liu et al., 2012; Wu et al., 2012; Zhang, 2011). However, since the initial condition typically exerts significant influences on short timescales within the earth system while parameters are more important on longer timescales (e.g., Branstator & Teng, 2010), constructing an error propagation model to project the model-data misfits onto both the initial condition and the parameters is difficult. Using an ensemble Kalman filter with short assimilation window (within predictability limit of the chaotic system), Zhang (2011) proposed to optimize the initial state first until the model-data misfits reach a quasi-equilibrium, where the parameter errors dominate; then they optimized the model parameters to reduce residual errors. Liu et al. (2012) used an adjoint model to project the model-data misfits over a large assimilation window onto the initial condition, atmosphere forcing, and the eddy mixing parameters.

Applications of SPE in the ocean models (Liu et al., 2012) and intermediate coupled models (Wu et al., 2012) have shown the added effects on mitigating model bias and improving the accuracy of the prediction. However, up to date, parameter estimation (Lu et al., 2021; Panteleev et al., 2020) and state estimation (e.g., Fenty et al., 2017;Forget et al., 2015; Lindsay & Zhang, 2006; Lyu et al., 2021b; Mu et al., 2018; Nguyen et al., 2021) are performed separately in the sea ice-ocean coupled model. As the rapid thinning of the Arctic sea ice and its extremely strong spatial heterogeneity, it is necessary to have parameters varying spatiotemporally with respect to the changing climate background. Therefore, we developed SPE in a sea ice-ocean coupled model and investigated its potential effects by assimilating satellite and in-situ measurements.

This paper is organized as follows. In Section 2, we introduce the coupled sea ice-ocean assimilation system, including the model configuration, the parameters being adjusted, as well as the assimilated and independent observations. Section 3 briefly evaluates the parameter sensitivities and accuracy of the adjoint model based on the tangent linear model. Section 4 discusses the added effects of SPE. At last, we summarize this study in Section 5.

2 Methodology

2.1 The Pan-Arctic Ocean and Sea Ice Assimilation System

The sea ice-ocean coupled assimilation system is based on the adjoint method (4D-Var in the operational oceanic and meteorological forecast communities) of the estimating the Circulation and Climate of the Ocean (ECCO) project, using the Massachusetts Institute of Technology general circulation model (MITgcm, Marshall et al., 1997) coupled with a zero-layer dynamic and thermodynamic sea ice model (Hibler, 1979; Hibler 1980; Losch et al., 2010). The sea ice dynamics are based on a viscous-plastic rheology and solved using a line successive over-relaxation algorithm (Zhang & Hibler 1997).

The adjoint of the sea ice-ocean coupled model is generated using the Transformation of Algorithms in Fortran (Giering & Kaminski, 1998; Heimbach et al., 2010). However, due to the persistent instability issue, the adjoint of the sea ice dynamics are usually excluded (Fenty & Heimbach, 2013; Fenty et al., 2017; Nguyen et al., 2021) or simplified to the adjoint of a free-drift sea ice dynamic (Koldunov et al., 2017; Lyu et al., 2021a; Lyu et al., 2021b) in assimilation experiments. Lyu et al. (2023) incorporated and approximated the adjoint of viscous-plastic sea ice dynamics and we use the same model configuration in this study. Horizontally, we use a curvilinear grid with a resolution of 12–18 km. Vertically, we have 50 z-levels ranging from 10 m at the surface to 456 m in the deep ocean. In this study, we further

https://doi.org/10.5194/gmd-2024-189
Preprint. Discussion started: 30 April 2025

Geoscientific Model Development
Discussions

developed the adjoint model for estimating the state and spatiotemporally-varying parameter jointly, and evaluated the added effects by comparing with the results in Lyu et al. (2023).

The adjoint method minimize a quadric form cost function (J) iteratively by adjusting the control variables (C) to bring the model simulation close to available observations:

$$J(C) = \sum_{t=1}^{T1}[y(t) - E(t)x(t)]^T R^{-2}[y(t) - E(t)x(t)] + CB^{-2}C^T \quad (1)$$

The first term on the right-hand side computes the "distance" between the observations (x) and the corresponding model-simulated variables (y) over a long period (one year in this study). The model-data misfits are normalized by their prior uncertainties (R) and E interpolates the model state to the observations. The values of R for different types of observations are introduced Section 2.2.

The second term on the right-hand side measures the size of the adjustments on the control variables (C) and B is the background error covariance. In the 3D-Var and 4D-Var system with short assimition windows (orders of days), constructing the matrix B^{-2} is critical for achieving the multivariate adjustments on initial conditions (Li et al., 2008; Weaver & Mirouze, 2013). In our study with a one-year assimilation window, we rely on the adjoint model (the first term on the right hand side) to project the model-data misfits on the control variables. Therefore, we assume B is diagonal and hence the background term mainly limits the sizes of the adjustments and ensures that complete information on the control variables.

In addition to the initial oceanic temperature and salinity, SIC, sea ice thickness (SIT), and daily atmosphere state, which includes 2-m air temperature, 2-m specific humidity, precipitation rate, 10-m wind vectors, downward longwave radiation, and net shortwave radiation, we further include 13 spatiotemporally-varying model parameters (see Table 1) in the control variables. These parameters vary depending on geographic locations and every day. The uncertainties of the 13 parameters are not known exactly and we set the uncertainties to 20% of their default values.

The assimilation system minimize the cost function J iteratively using a quasi-Newton algorithm (Gilbert & Lemaréchal, 2006) and the gradient information $\frac{\partial J}{\partial C}$. The optimization stops until the cost function cannot be further reduced. The adjoint of the ocean-sea ice coupled model is used to compute $\frac{\partial J}{\partial C}$ with dimensions of 10^8. To guarantee the stability of the adjoint model for a period of one year, modifications on the adjoint codes are treated delicately. Details are given in Lyu et al. (2023). The accuracy of the adjoint model is shown in Section 3.

2.2 The Assimilation Experiments and the Control Variables

Two assimilation experiments and one control run are performed to examine the added effects of SPE. The initial condition on January 01 2012 is taken from the Arctic sea ice-ocean reanalysis of Lyu et al. (2021b), which uses the same model configuration as in this study. We take the forward simulation at iteration 0 as the control run (CTRL). The two assimilation experiments are different in their choice of the control variables. In the first assimilation experiment, we only adjust the initial conditions and atmosphere forcings (named opti-SE hereinafter). In the second assimilation experiment, we further include 13 spatiotemporal-varying model parameters (see Table 1 for details) in the control variables (named opti-SPE). To avoid the over-adjustments on the parameters, which may result in the model instability, we further set the upper and lower bounds for individual parameters in the model codes.

https://doi.org/10.5194/gmd-2024-189
Preprint. Discussion started: 30 April 2025

Geoscientific Model Development Discussions

Table 1. The sea ice model parameters applied for optimization

Parameters	Description	Default Values	Lower/Upper bounds
α_{wice}	Albedo of melting ice	0.66	0.50, 0.95
α_{dice}	Ice albedo	0.75	0.50, 0.95
α_{wsnow},	Albedo of melting snow	0.71	0.50, 0.95
α_{dsnow}	Snow albedo	0.83	0.50, 0.95
$Cond_{ice}$	Ice conductivity($W \cdot m^{-1} \cdot K^{-1}$)	2.17	1.50, 3.00
$Cond_{snow}$	Snow conductivity($W \cdot m^{-1} \cdot K^{-1}$)	0.31	0.15, 0.40
C_{d_wind}	Wind-ice drag coefficient	2.0×10^{-3}	1.0×10^{-3}, 5.0×10^{-3}
C_{d_water}	Water-ice drag coefficient	5.5×10^{-3}	1.0×10^{-3}, 10.0×10^{-3}
H_o	Lead closing parameter, which determines the minimum sea ice thickness formed in open water (m)	0.5	0.03, 1.0
$P*$	Ice compressive strength constant (N m^{-2})	2.8×10^{4}	1.0×10^{4}, 5.0×10^{4}
$C*$	Ice strength decay constant	-20.0	-30.0, -5.0
Es	Eccentricity of the yield curve describing the viscous-plastic rheology	2.0	1.5, 2.3
F_T	Friction velocity for ice-ocean heat flux (m s^{-1})	0.88×10^{-3}	0.4×10^{-3}, 1.2×10^{-3}

2.2 Assimilated Observations

We assimilate both satellite and in-situ observations (listed in Table 2). In the assimilating process, the observations and their uncertainties must be provided beforehand. Uncertainties for these type of observations are described in previous studies (Lyu et al., 2023).

Altimeter along-track L3 sea surface heights anomalies (SLA) are assimilated with observational uncertainties of 3 cm. The gridded sea surface temperature (SST) data for the open waters and its uncertainties are based on optimal interpolated microwave and infrared data from the Remoting Sensing System (Gentemann et al., 2004). Oceanic temperature and salinity data is based on EN4 dataset (Good et al., 2013). Uncertainties of temperature and salinity (T&S) profiles are depth-dependent, ranging from ~0.6 °C and ~0.3 PSU at the surface to ~0.02 °C and ~0.02 PSU in the deep ocean. World Ocean Atlas 2018 (WOA18) climatology is also assimilated to reduce the bias in ocean temperature and salinity and their prior uncertainties are set to five times of the in-situ profiles. Since we interpolate the WOA18 to the finer model grids, we further reduce the weight of temperature and salinity climatology cost components by multiplying a factor of 0.04.

We assimilate the ASI-SSMI SIC dataset (Kaleschke et al., 2001; Spreen et al., 2008). This dataset doesn't provide uncertainty estimates. In data assimilation study, the uncertainties should consist of representation and instrumental uncertainties. Considering the dependence of SIC product uncertainty on absolute value of SIC (Chen et al., 2023) and larger SIC uncertainties off the coast due to the poor accuracy in the SIC product and the poor representation of landfast ice in the model (Fenty & Heimbach, 2013), we use spatiotemporally varying SIC uncertainties. In the implementation, background uncertainties are assumed to be 15% within 50 km from the coastline and 10% in the other area, which represents the spatial pattern of the representation uncertainties. Then, we multiply

Geoscientific Model Development Discussions
Open Access
EGU

the background uncertainties with factors of 0.85, 1.20, 1.10, and 1.00 for the observed SIC ranges of 0%, <15%, 15%-25%, and >25%, respectively.

Satellite SIT data used is based on the merged CryoSat-2 and SMOS product (CS2SMOS) with estimates of uncertainties (Ricker et al., 2017). The SIT in this dataset represents the mean SIT over 25 km×25 km areas but excludes open waters. Note that the model simulates the effective SIT (SIT×SIC), we convert the effective SIT to the gridded SIT and then compare it against the satellite SIT observations in the cost function. Satellite sea ice drift (SID) data is derived from the Ocean & Sea Ice Satellite Application Facility (OSISAF, https://osi-saf.eumetsat.int) product at a resolution of 62.5 km, which applies a continuous maximum cross correlation method to track the sea ice displacements over a period of 48h from sequence of satellite images (Lavergne et al., 2010). The uncertainties are dominated by satellite resolution (10–15 km), which are set to 10 km every 2 days (~0.06 m s^{-1}).

Table 2. Assimilated Observations.

Datasets	Resolution	Number	Source	Reference
SLA	7.0 km	7.6×10^5	http://marine.copernicus.eu	(Pujol et al., 2016; Taburet et al., 2019)
SST	25.0 km	2.0×10^7	https://data.remss.com/SST/daily/mw_ir/v05.1/netcdf/, (last access: 13 April 2025)	(Gentemann et al., 2004)
T&S	–	5.0×10^5	https://www.metoffice.gov.uk/hadobs/en4/download-en4-2-2.html, (last access：13 April 2025)	(Good et al., 2013)
SIC	25.0 km	3.6×10^7	https://thredds.met.no/thredds/catalog/osisaf/met.no/reprocessed/ice/conc_450a_files/catalog.html (last access：13 April 2025)	(Lavergne et al.,2019)
SIT	25.0 km	8.9×10^6	https://spaces.awi.de/display/CS2SMOS/CryoSat-SMOS+Merged+Sea+Ice+Thickness (last access：13 April 2025)	(Ricker et al., 2017)
SID	62.5 km	5.8×10^5	https://thredds.met.no/thredds/catalog/osisaf/met.no/ice/drift_lr/merged/catalog.html (last access: 13 April 2025)	(Lavergne et al., 2010)
WOA18	1°	2.9×10^7	https://www.ncei.noaa.gov/access/world-ocean-atlas-2018/ (last access: 13 April 2025)	(Locarnini et al., 2018; Zweng et al., 2018)

2.3 Independent Observations

Independent sea ice observations are used to validate the assimilation results. The observations can be categorized into two groups: 1) single-point measurements which includes sea ice variables within a small area or sites, including SIT or snow depth obtained by the Ice Mass Balance buoys (IMBs) and ice draft from the mooring upward looking sonar (ULS); 2) gridded measurements such as the remote sensing. These two different measurements are not fully consistent, especially in regions with strong ice spatial heterogeneity and prevalent ice dynamic processes. Nevertheless, we use these data to validate and cross-validate the assimilation results and gridded SIT observations, identifying potential discrepancies of the assimilated datasets, the numerical model, and the point observations.

2.3.1 Ice Mass Balance Buoy

IMB is an ice-based observing system which measures the evolution of snow and sea ice growth and ablation, vertical temperature profiles through the snow, ice, and upper ocean along the ice drift trajectory. It uses two acoustic

https://doi.org/10.5194/gmd-2024-189
Preprint. Discussion started: 30 April 2025

sensors to measure the ice surface and bottom and therefore SIT is derived by the distance of ice surface and bottom. The uncertainty of ice surface and bottom measured by the each acoustic sounders is ±5mm (Richter-Menge et al., 2006). The IMBs are deployed on thick and level ice floe to achieve the relative long measurement and ensure spatial representativeness of observations. It must be acknowledged that directly comparing this point measurements of SIT with the gridded SIT is not fully straightforward. Thus, we also compare the mean SIT bias, and SIT temporal changes along the drifting trajectories. Compared to the satellite or helicopter-based altimeter observations, the IMB observations can effectively characterize the thermodynamic thickening of sea ice (Koo et al., 2021; von Albedyll et al., 2022).

2.3.2 International Arctic Buoy Programme

The International Arctic Buoy Programme (IABP, https://iabp.apl.uw.edu/index.html) collects ice-based drifting buoys from different organisations. Most of these buoys also monitor sea level pressure, surface air temperature along the ice drift trajectories. In this study, we compute sea ice velocities based on drift trajectories, which is then compared with the model simulations. In 2012, we selected 23 trajectories with continuous position observations more than 100 days for the model validation.

2.3.3 Mooring measurements from the Beaufort Gyre Exploration Project

Starting from 2003, the Beaufort Gyre Exploration Project (BGEP) based at the Woods Hole Oceanographic Institution (https://www2.whoi.edu/site/beaufortgyre/) deployed upward looking sonar (ULS) at three locations of Ma, Mb, and Md (see Figure 7). The ULS measures local sea ice draft with an error of ±0.1m (Krishfield et al., 2014) throughout the year. In this study, we use the daily-averaged sea ice draft for comparisons. The sea ice drafts are converted to sea ice thickness by multiplying with a factor of 1.1 which is calculated as the ratio between mean sea water of 1024.0 kg m^{-3} and sea ice density of 910.0 kg m^{-3}, assuming no snow on sea ice (Nguyen et al., 2011).

3 Parameter Sensitivities and Accuracy of the Tangent Linear Approximation

There are two prerequisites for optimizing the model parameters with observations. Firstly, the parameter changes within the range of uncertainties have considerable impacts on the model simulation. For instance, the SIC perturbations caused by parameter uncertainties are larger than observation uncertainty. Secondly, the error propagation model (the tangent linear model in this study) should reproduce the spatiotemporal error propagations induced by the model uncertain inputs accurately.

Here, we perturb the 13 model parameters (see Table 1) by 10% and integrate the model for the year 2012. Then we evaluate the spatiotemporal changes in SIC normalized by satellite SIC observational uncertainties (e.g., 15%). Values of normalized SIC changes >1.0 indicate that the SIC changes caused by 10% perturbations on the parameters can be detected by satellite observations. As Figure 1 shows, the albedos of the dry/wet snow and ice (α_{dsnow}, α_{dice}, α_{wsnow}, α_{wice},) have pronounced impacts on the summertime SIC. Wind-ice drag coefficients (Cd_{wind}) and ice

https://doi.org/10.5194/gmd-2024-189
Preprint. Discussion started: 30 April 2025

Geoscientific Model Development
Discussions

compressive strength constant (P^*) also show large impacts throughout the year. For the other parameters, the normalized SIC changes grow slowly and show little dependence on the seasonality.

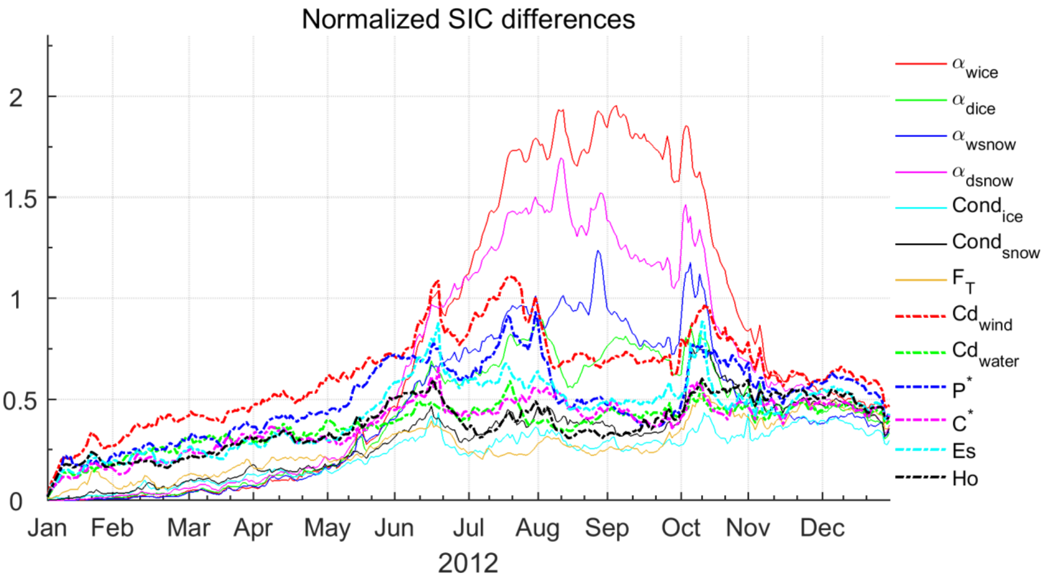

Figure 1. Temporal evolutions of the norm of the SIC differences (normalized by 15% SIC) averaged over the ice-covered regions due to the 10% perturbations on the 13 parameters (see Table 1 and the legend).

The accuracy of the tangent linear approximation is examined based on the Taylor expansion. Taking the parameters H_o as an example, we perturb it by $\Delta H_o = 10\% \times H_0$ and evaluate the first-order and higher approximation as follows:

$$\boldsymbol{\Delta X_1 = M(H_o + \Delta H_o) - M(H_o) = \frac{\partial M}{\partial H} \cdot \Delta H_o + o(\Delta {H_o}^2)} \quad (2),$$

$$\textbf{and } \boldsymbol{\Delta X_2 = M(H_o - \Delta H_o) - M(H_o) = -\frac{\partial M}{\partial H} \cdot \Delta H_o + o(-\Delta {H_o}^2)} \quad (3).$$

Here, M is the model operator and X represent the model variables. The linear (first-order) and nonlinear (higher-order) errors can be obtained by $\frac{1}{2}(\Delta X_1 - \Delta X_2)$ and $\frac{1}{2}(\Delta X_1 + \Delta X_2)$. By integrating the tangent linear model with $\Delta H_o = 10\% \times H_0$, we get error evolution of the model variables.

Although the overall impacts of H_o on SIC do not exceed the SIC observational uncertainties (normalized SIC changes <1.0, Figure 1) over the one-year period, it has large impacts over the open water during the refreezing time (Figure 2a). Since H_o determines the initial sea ice thickness formed in open water, increasing H_o by 10% will delay the formation of new ice over the open water, resulting in the reduced sea ice coverage over the Arctic Ocean. The signals are dominated by the linear component (Figure 2a) and the nonlinear component is small (Figure 2b). The tangent linear model can reproduce the negative SIC changes very well (Figure 2c).

https://doi.org/10.5194/gmd-2024-189
Preprint. Discussion started: 30 April 2025

Geoscientific Model Development Discussions

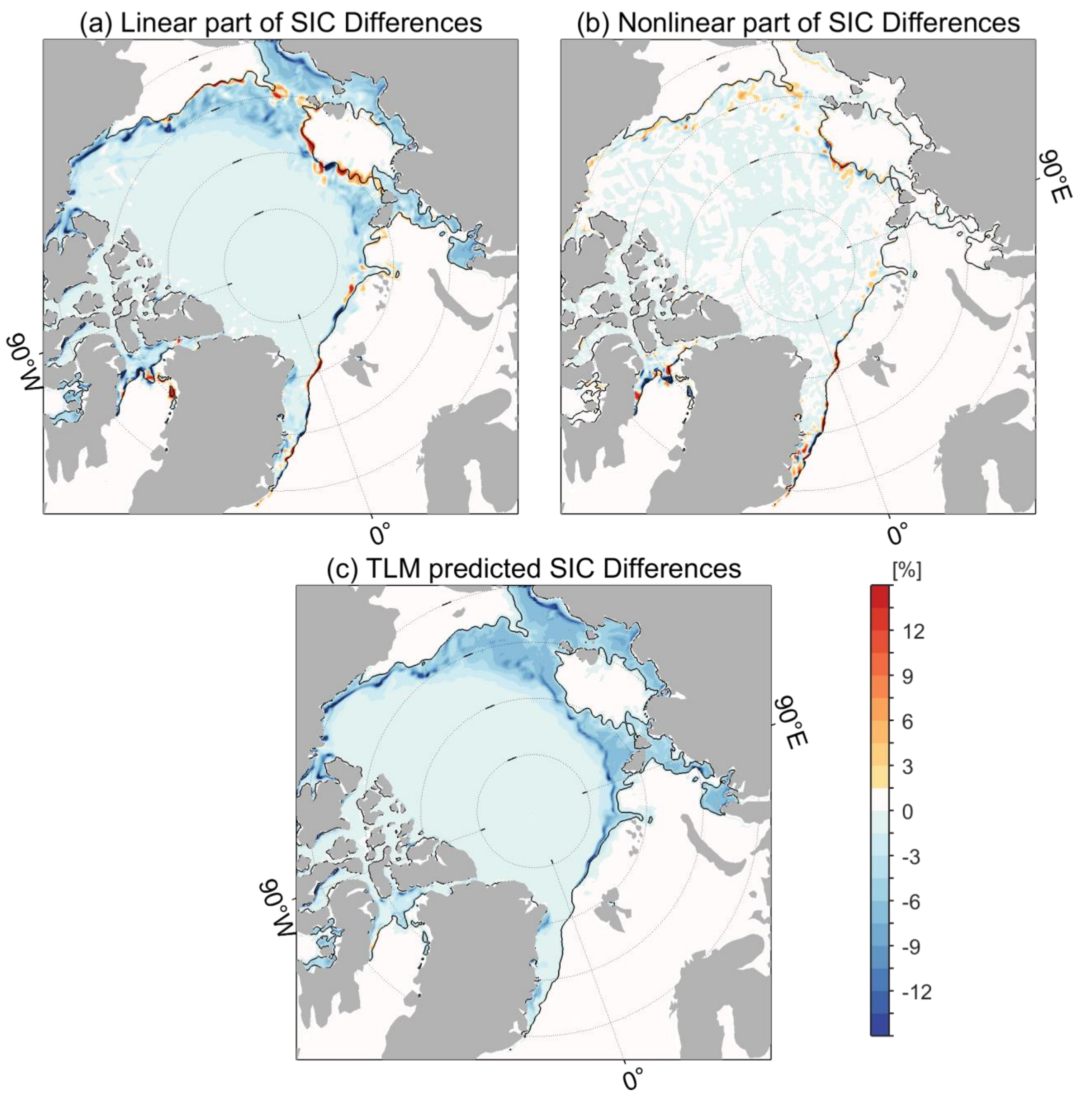

Figure 2. (a) The linear and (b) nonlinear parts of SIC differences on November 11 2012. Panel (c) is the corresponding SIC changes predicted by the tangent linear model. The black lines denote the 15% SIC contour.

The above analysis demonstrates that the responses of SIC to parameter perturbations are dominated by the linear component, and that the tangent linear model represents the linear component of the error propagation well with corresponding pattern and amplitude. The results motivate us to further explore the potential of using observations to estimate the state and parameters simultaneously.

https://doi.org/10.5194/gmd-2024-189
Preprint. Discussion started: 30 April 2025

Geoscientific Model Development Discussions

4 Evaluation of the Assimilation Results

In this section, we evaluate the impacts of SPE on the estimated sea ice state. Besides, we compare the two assimilation runs and the control run against independent observations.

4.1 The cost function reduction

The optimization algorithm reduces the cost function (Equation 1) iteratively using the gradients $\frac{\partial J}{\partial c}$. In the opti-SE and opti-SPE, the optimizations stop at iterations 32 and 86, respectively. The cost functions are reduced to 59.8% and 49.3% (Figure 3), and the norms of the gradients ($\left|\frac{\partial J}{\partial c}\right|$) are reduced to 10.7% and 9.0%, respectively.

Of the assimilated observations, the daily SST and SIC contribute to 27.3% and 42.9% of the cost function, which are reduced to 14.0% and 19.4% in opti-SE and to 10.1% and 13.2% in opti-SPE. For other observations, their cost components are also reduced slightly. In the following part, we will focus on the improvements on the SIC, SIT, and SID, and evaluate the simulations with independent observations.

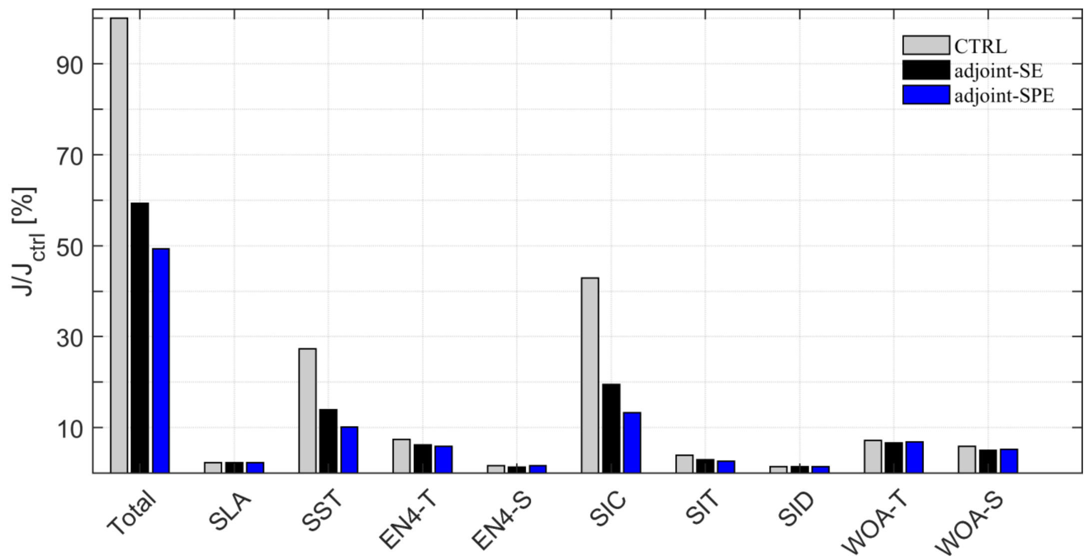

Figure 3. The total cost function and individual components normalized by the total cost function in the control run (Jctrl). Abbreviations: SLA—sea level anomalies, SST—sea surface temperature, EN4-T—EN4 temperature profiles, EN4-S—EN4 salinity profiles, SIC—sea ice concentration, SIT—sea ice thickness, SID—sea ice drift velocities; WOA—T and WOA—S, climatological temperature and salinity from WOA18 dataset.

4.2 Improvements on Sea Ice Concentration

Satellite observations have been widely assimilated into coupled sea ice-ocean models to improve the simulated-SIC (e.g., Lindsay & Zhang, 2006) and the other model prognostic variables (e.g., Lyu et al., 2021b; Lyu et al., 2023; Mu et al., 2018; Nguyen et al., 2021).

In the control run, the normalized SIC errors grow quickly during spring and reach a maximum in June. Then the SIC errors decrease from July to September and increase drastically again during October (grey line in Figure 4). opti-SE greatly improves the simulated SIC with the normalized SIC errors close to 1.0 throughout the year (black line in

Figure 4). Still, there are notable SIC errors from May to June. During October when the ocean starts to refreeze, the drastic increase of SIC errors is not reduced. By optimizing the model parameters jointly, opti-SPE further brings down the SIC errors, especially, the errors from May to June and during October were brought to an acceptable level (solid blue line in Figure 4).

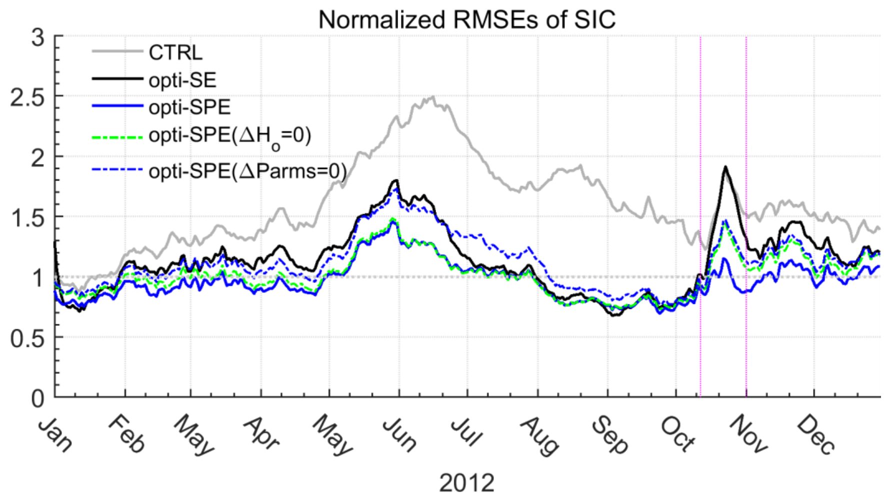

Figure 4. Seasonal evolution of the root mean square errors of SIC (normalized by prior uncertainties) in CTRL, opti-SE, and opti-SPE. In opti-SPE (ΔHo=0), we replace the optimized Ho to its default value. And in opti-SPE (ΔParms=0), we replace all the 13 parameters to their default value.

Another two simulations are presented in Figure 4, which demonstrates the added effects of estimating parameters jointly. By replacing all the 13 parameters to their default values, SIC errors increase to a similar level as in opti-SE (dashed blue line in Figure 4). However, in October, the SIC errors are smaller than opti-SE when we reset the 13 parameters to their default values. That indicates that the data assimilation find a smaller minima of the cost function J which is blocked in opti-SE. The further improvements in opti-SPE after October are partially attributed to adjustments on the parameter H_o, seen as the drastic SIC errors increase when setting ΔH_o=0 (opti-SPE (ΔH_o=0), dashed green line in Figure 4).

We now focus on the SIC improvements during October. The SIC differences between the control run and satellite observations are pronounced in the Pacific sector of the Arctic Ocean (enclosed by dashed black line in Figure 5a-c), where sea ice loss in summer is the most prounced over the Arctic Ocean. At the beginning of October, the Pacific sector is ice-free (red line in Figure 5d). The control run fails to reproduce the ice-free conditions (grey line in Figure 5d), while both opti-SE and opti-SPE reproduce the ice-free conditions well (black and blue lines in Figure 5d). Starting from October 10, the sea ice starts to recover. Compared with the control run and the observations, opti-SE underestimates SIC by more than 40% (Figure 5b), and the underestimation persists until the early November (Figure 5d). By adjusting the model parameters simultaneously, opti-SPE improves the sea ice recovery process and reduces the negative SIC bias successfully (Figure 5c, d).

https://doi.org/10.5194/gmd-2024-189
Preprint. Discussion started: 30 April 2025

Geoscientific Model Development
Discussions

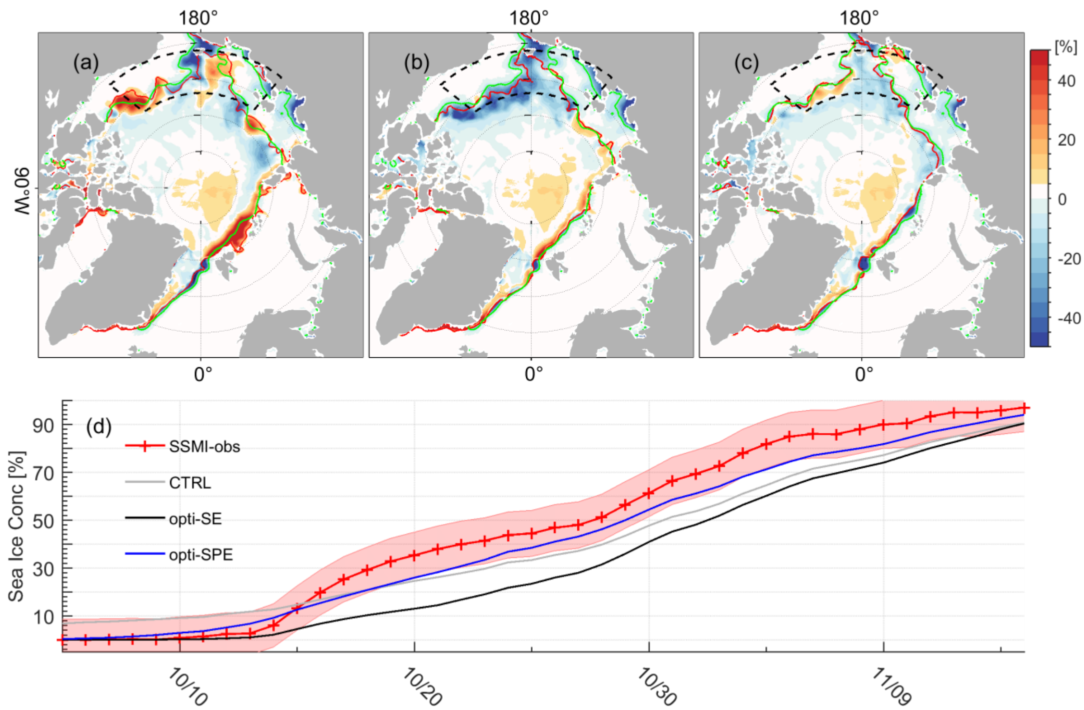

Figure 5. Model-data differences of SIC averaged from October 12 to October 22 in (a) CTRL, (b) opti-SE, and (c) opti-SPE. (d) Temporal evolution of in SIC averaged over the Pacific sector (enclosed by the dashed black line in panels (a)–(c)).

During the summer season, the open waters accumulate a large amount of heat and these ocean heat must be released before ocean surface refreezes. Since the control run fails to reproduce the ice-free conditions (Figure 5d), more sea ice appears in the Pacific sectors of the Arctic Ocean and less ocean heat needs to be released before open water surface refreezes. However, due to the ice-free conditions in the summer season in opti-SE and opti-SPE, the ocean need to release more heat before refreezing. Therefore, opti-SE shows much slower sea ice growth rate initially. While, opti-SPE adjusts the parameters H_o to improve the SIC simulation. In the sea ice model, H_o is the minimum SIT formed in open water, which impacts vertical and lateral growth of the sea ice and is set to 0.5 m by default. Over the ice-free water, decreasing H_o reduces the amount of latent heat needs to be released during the initial formation process of sea ice. And after the initial formation, the decreased H_o leads to faster formation of thinner sea ice over the open water area. In opti-SPE, H_o is reduced by more than 0.1 m for the open water (Figure 6a) at the onset of refreezing (Figure 6b), which gives rise to the rapid growth of thinner sea ice. The quick sea ice recovery would reduce the heat and momentum exchanges between atmosphere and ocean evidently, thereby changing the feedback process in the atmosphere-sea ice-ocean system.

https://doi.org/10.5194/gmd-2024-189
Preprint. Discussion started: 30 April 2025

Geoscientific Model Development
Discussions

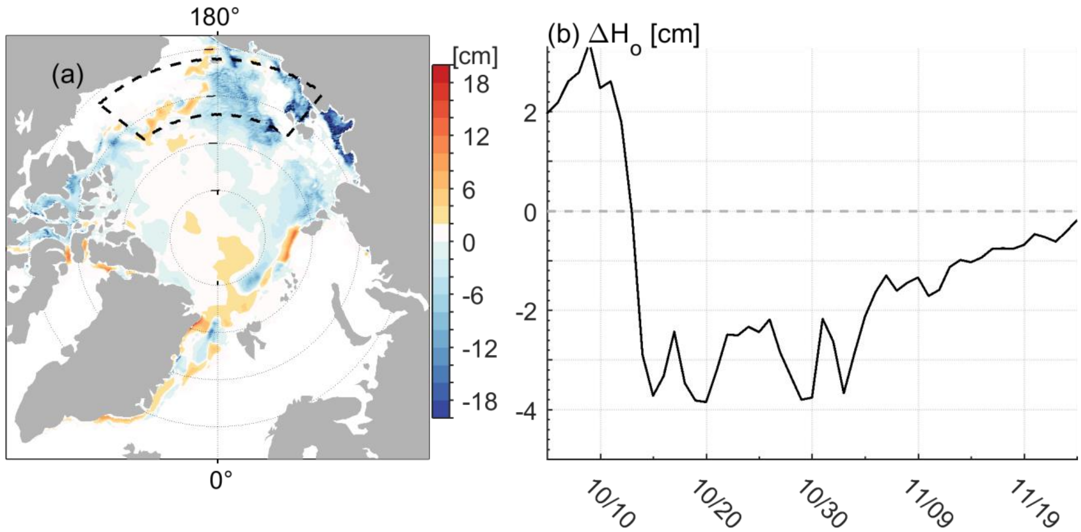

Figure 6. (a) Adjustment on the parameter H_o (in cm) averaged from October 12 to October 22. (b) Temporal changes in adjustments of H_o averaged over the Pacific sector (enclosed by the dashed black line in (a)).

4.3 Comparisons against Independent Observations

4.3.1 Measurements at BGEP Moorings

We interpolated the gridded SIC and SIT data to the BGEP mooring locations to explored their seasonal variations.

The sea ice extent in 2012 reached the unprecendented low values since the satellite era. The ULS of three moorings also observed ice-free conditions from August to October. The control run fails to simulate the ice-free conditions while both opti-SE and opti-SPE reproduce the seasonal SIC variation successfully (Figures 7a–c). The opti-SPE shows smaller RMSE at M_b and M_d than opti-SE and CTRL (see the numbers in Figure 7b, c). In opti-SPE, an pack ice break off from the main ice field from July 20 to the early August and is gradually melted at M_a, resulting in the slightly larger RMSEs (Figure 7a).

For SIT, the two assimilation runs bring the simulated-SIT into consistency with the CS2SMOS observations (Figure 7d–f) and the ULS-measurements. From January to August, the gridded SIT (the CS2SMOS and the two assimilation runs) agree well with the ULS-measured SIT, since the Beaufort Sea is covered by compact ice. However, from October to December when the open ocean starts to refreeze, the CS2SMOS, the two assimilation runs, and the ULS-measurements show systematic discrepancies. The SIT increases more quickly in CS2SMOS dataset than the two assimilation runs and the ULS-measurements. The two assimilation runs generate the smallest error against the ULS-observed SIT and satellite-observed SIC at the three mooring locations, within the prior observational uncertainties.

https://doi.org/10.5194/gmd-2024-189
Preprint. Discussion started: 30 April 2025

Geoscientific Model Development
Discussions

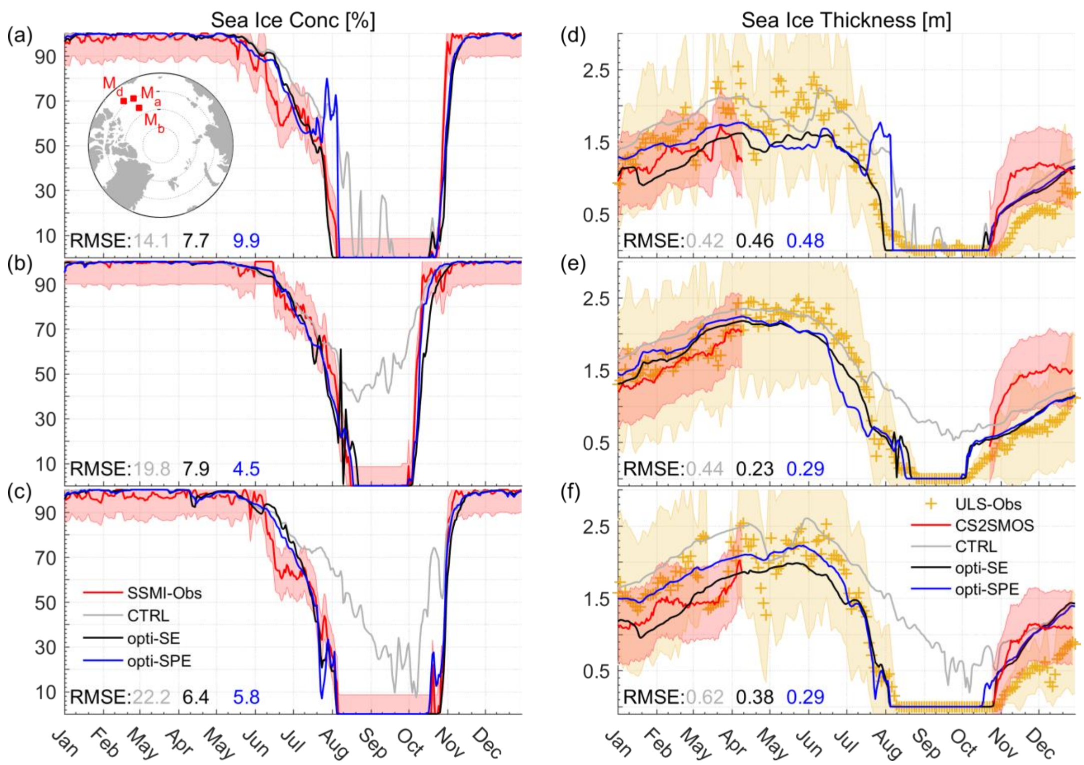

Figure 7. SIC from satellite observations (SSMI-Obs), CTRL, opti-SE and opti-SPE at the mooring locations (a) Ma, (b) Mb, and (c) Md (see locations in subplot of panel (a)). The RMSEs of SIC between the three simulations and SSMI-Obs are listed in panels (a)–(c). Panels (d)-(f) are the corresponding SIT derived from the upward looking sonar (ULS-Obs), CS2SMOS, CTRL, opti-SE, and opti-SPE. And the RMSEs of SIT between the three simulations and ULS-Obs are also listed in panels (d)–(f). The shadings indicate the uncertainties of satellite SIC and SIT obervations. For the ULS-Obs, we use the standard deviation of sub-daily sea ice thickness to represent the uncertainties.

4.3.2 SIT from IMB data

The IMBs measure the variation of SIT along the drift trajectories. Comparing these Lagrangian SIT observations with the gridded SIT from sea ice-ocean coupled model and satellite is less straightforward since the comparisons are usually subject to biases (e.g., Mu et al., 2018). We choose two metrics for validation: 1) the mean SIT over the observing time; 2) central root mean square deviation (CRMSD), computed as $\sqrt{\frac{1}{N}\sum_1^N\left((x_n-\overline{x_n})-(y_n-\overline{y_n})\right)^2}$, where *x* and *y* represent the simulated- and measured-SIT, respectively, and the overbar denotes time average. The smaller CRMSD values, the better the simulation reproduces the sea ice evolution. We selected six IMBs with long living records: one of them was deployed in 2011 in the central Beaufort Sea (2011J) and drifted toward the Chukchi Sea (top left panel in Figure 8) in 2012; the other five IMBs are deployed in 2012 in the central Arctic.

https://doi.org/10.5194/gmd-2024-189
Preprint. Discussion started: 30 April 2025

Geoscientific Model Development
Open Access
Discussions

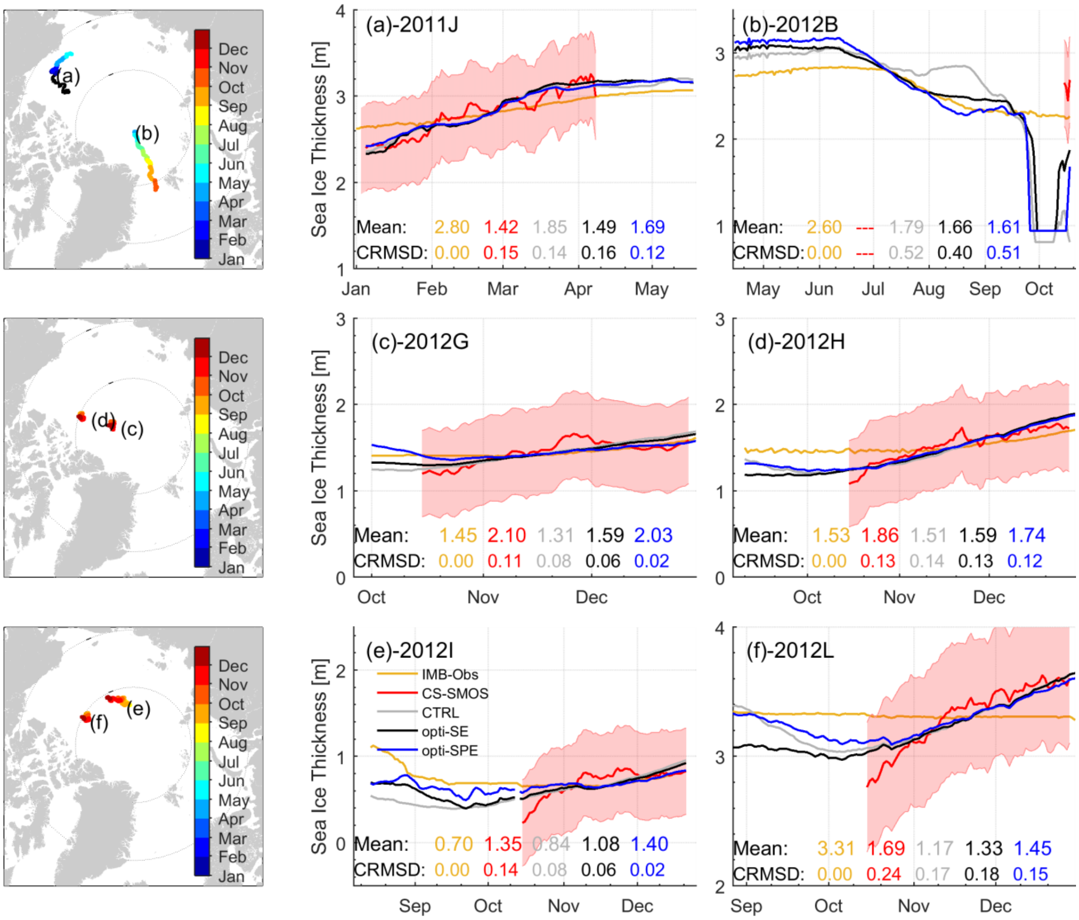

Figure 8. SIT along the IMB trajectories. The IMB trajectories (a-2011J, b-2012B, c-2012G, d-2012H, e-2012I, f-2012L) are shown in the left panels and the colors indicate the observing time. The SIT of IMBs (yellow lines), CS2SMOS (red lines), CTRL (grey lines), opti-SE (black lines), opti-SPE (blue lines) are plotted in the right-hand side against observing time. The shadings indicate the CS2SMOS observational uncertainties. The statistics (mean SIT and CRMSD against IMBs) of IMBs, CS2SMOS, CTRL, opti-SE, and opti-SPE are also shown in each plot.

SIT biases of 0.2–0.7 m appear between the CS2SMOS data and the control run. The optimization brings the model simulations close to the CS2SMOS data, especially in opti-SPE (“Mean” values in Figure 8c–f). Considering the SIT evolution along the drift trajectories, both opti-SPE and opti-SE reproduce the seatellite-measured sea ice growth processes well.

As expected, the IMB measurements are usually show 0.5–1.5 m biases compared with the CS2SMOS observations (Figure 8) which likely indicates that the IMB deployment site with the ice condition don’t necessarily represent a large spatially average, especially SIT. Considering the SIT variation along the drift trajectories, the three model simulations and the IMB measurements show much weaker SIT variabilities than the CS2SMOS observations because of 1) the buoys is generally deployed on the relatively thick level ice (Richter-Menge et al., 2006), and 2) the satellite altimeter observations contain a large amount of signal from the thin ice, which has a relatively large growth

https://doi.org/10.5194/gmd-2024-189
Preprint. Discussion started: 30 April 2025

rate (Lei et al., 2022), and ice dynamic deformation can also contribute to the thickening of sea ice within the grid (von Albedyll et al., 2022). The CRMSD, computed between the gridded SIT with the IMB measurements, show that the SIT variations in opti-SPE matches the best to the IMB measurements.

In summary, opti-SPE effectively reduces the mean SIT biases between CS2SMOS observations and the control run. The two assimilation runs reproduce the SIT variation observed by IMBs, with CS2SMOS observations exhibiting greater variability than IMB measurements. Analysis of the CRMSDs reveals that opti-SPE matches sea ice evolution best with respect to the IMB measurements. We note that the data derived from point-measurements of IMB also have their own shortcomings, including the representativeness of initial ice thickness at the deployment, the impact of spatial heterogeneity of snow accumulation during the later measurement stages, and the inability to include sea ice thickening caused by ice dynamic deformation.

4.5 Sea Ice Velocity from IABP

Twenty-two IABP ice drifting buoys with drifting periods larger than 100 days are used the retrieve ice velocity, which are compared against the three model simulations. The buoys are deployed on the multi-year sea ice initially and then drift with the sea ice. Daily sea ice velocities are computed based on the buoy locations and the model-simulated sea ice velocities are interpolated to the buoy locations. We summarize the statistics, including the standard deviations, the correlation coefficients, and the root mean square deviations (RMSDs), with the Taylor diagrams (Taylor, 2001).

https://doi.org/10.5194/gmd-2024-189
Preprint. Discussion started: 30 April 2025

Geoscientific Model Development
Discussions

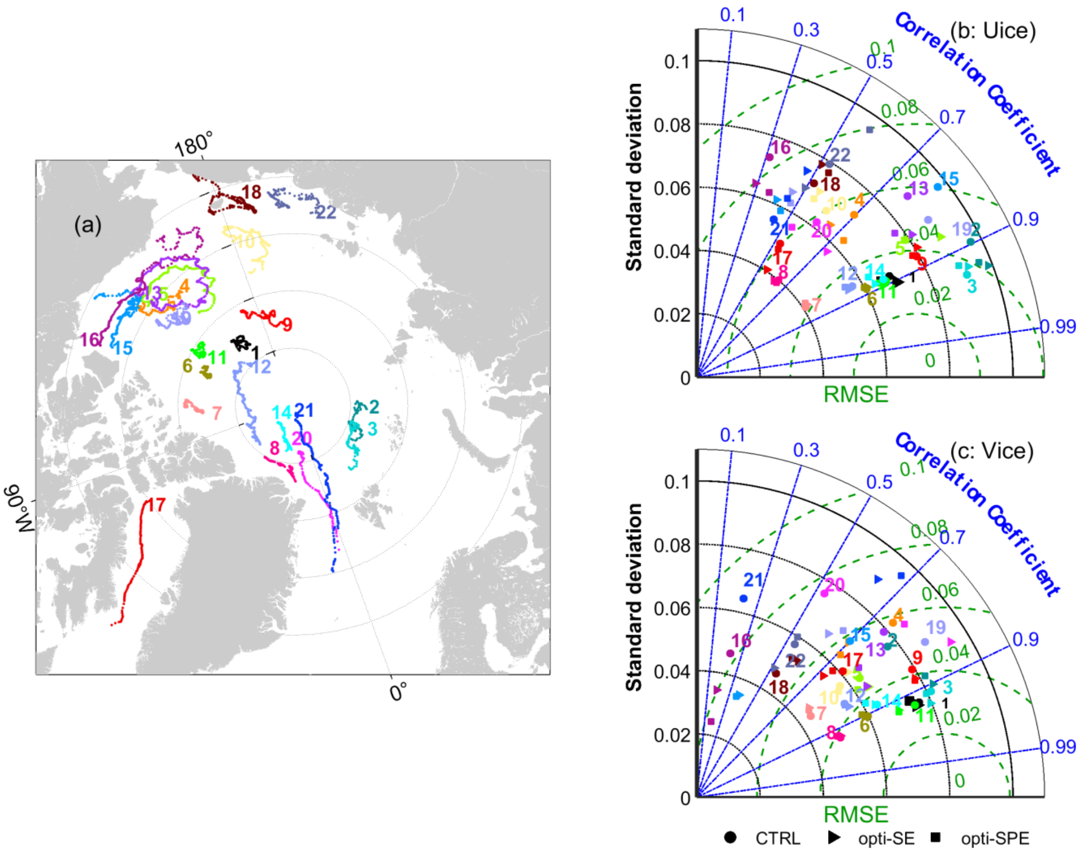

Figure 9. (a) IABP buoy trajectories in 2012. Taylor diagrams of CTRL (filled circles), opti-SE (filled triangles), and opti-SPE (filled squares) with respect to the (b) zonal (UICE) and (c) meridional (VICE) ice velocities retrieved from the IABP buoys.

The cost component of SID accounts for 1.45% of the total cost function, which is slightly reduced to 1.42% and 1.43% in opti-SE and opti-SPE, respectively. As shown in Figure 8b and c, the statistics of CTRL, opti-SE, and opti-SPE with respect to the zonal and meridional sea ice velocities from the drifting buoys show slightly differences. As from the statistics, these buoys can be categorized into two groups: 1) the buoys drifting in regions with compact ice (NO. 1-14 in Figure 9a); and 2) the buoys drifting into the region with low SIC gradually (NO. 15-22 in Figure 9a).

In the first groups (1-14 in Figure 9a), the RMSEs (0.0429, 0.0417, 0.0423) and correlation coefficients (0.8226, 0.8232, 0.8229) of CTRL, opti-SE, and opti-SPE are similar. For individual buoys, their statistics in the Taylor diagrams (Figure 9b, c) are also very close in CTRL, opti-SE, and opti-SPE, and the root mean square errors are mostly smaller than prior uncertainties (0.06 m s^{-1}).

Unlike the first group, the simulated ice velocities match the buoy observations (NO. 15-22 in Figure 9a) much worse in the second groups, with RMSEs of 0.0880, 0.0973, 0.0959 and the correlation coefficients of 0.5691, 0.4863, 0.4911 in CTRL, opti-SE, and opti-SPE. Besides, the statistics of the second groups in the Taylor diagrams are more dispersed, which indicates that two assimilation runs increase the sea ice velocity errors and degrade the correlations.

https://doi.org/10.5194/gmd-2024-189
Preprint. Discussion started: 30 April 2025

Geoscientific Model Development Discussions
Open Access

In Figure 10, we further analyze two buoy representatives (NO. 16 and 21 in Figure 9a) which gradually drifted toward the ice edge. The buoy-16 was deployed on April 12 2012 in the southeastern Beaufort Sea (72.38 °N, -127.47 °E), which drifted westward along the south periphery of the Beaufort Gyre, and ceased the data reporting by November 10 2012 at the Alaska coast (71.34 °N, -160.55 °E). The buoy-21 was deployed on April 15 2012 in the central Arctic Ocean. It was advected along the transpolar stream and out through the Fram Strait, and finally ceased the data reporting by November 06 2012 in the Greeland Sea.

The sea ice velocity differences are very small over regions with compact ice because the ice internal stress would attenuate the response of ice motion to wind forcing. Toward the marginal ice zone, SIC decreases from ~100% to 0 (Figure 10a, d) together with reduced ice internal stress. Sea ice is therefore becoming more sensitive to wind stress (Figure 10b-f). The sea ice velocity differences are very small over regions with compact ice. At the sea ice marginal zone, it is not possible for the three model simulations to reproduce the weakening ice field perfectly upon current sea ice model physics, resulting in visible errors in sea ice velocities. Along the buoy-16 trajectory, the satellite-observed SIC approached near zero by the early August (Figure 10a) while the buoy still drifted independently until the end of October (Figure 10b, c). During this period, the sporadic ice floes, including the ice floe with the buoy, cannot be detected by the satellite passive microwave observation; while the fragmented ice floes should enter a complete free-drift state, which means that the speed ratio of sea ice motion to wind reaches the maximum (e.g., Zhang et al., 2022). This ice condition increases the comparison uncertainty. We also suspect that the size of the ice floe with the buoy is too small to be captured by the satellite and the numerical model with resolutions of ~10 km. Therefore, the numerical simulation of sea ice and the characterization of heat and momentum exchange between the atmosphere and the ocean are extremely challenging for the margional ice zone.

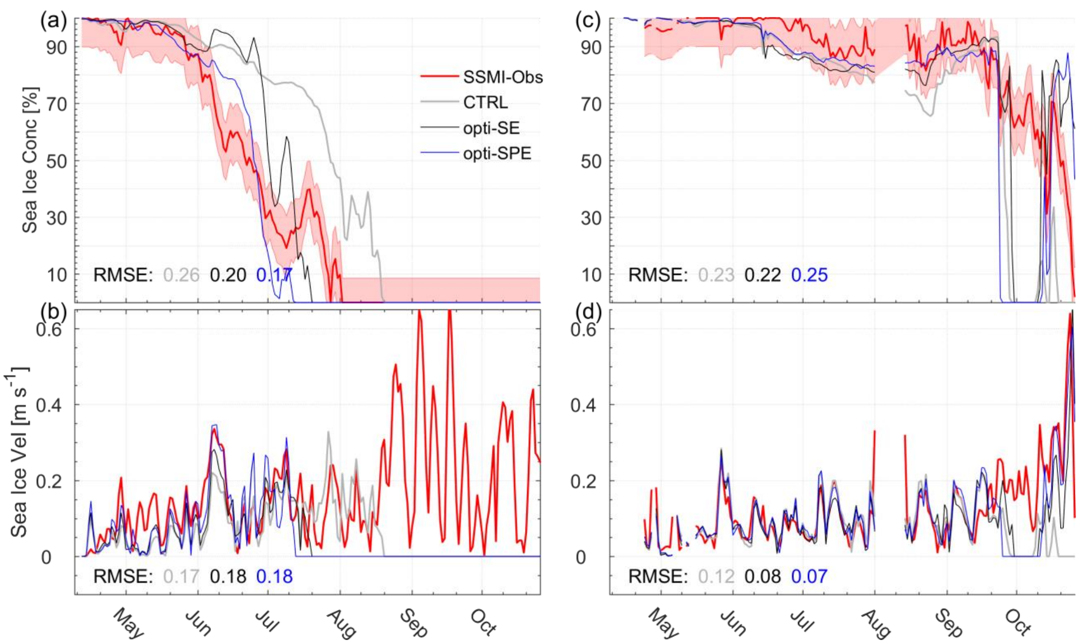

Figure 10. Changes in (a, c) SIC and (b, d) sea ice velocity along the buoy trajectories (NO. 16 and 21 in Figure 9a).

5 Conclusions and Discussion

In the coupled sea ice-ocean model, the parameters in the parameterization schemes describes the physical properities of the ocean and sea ice. Uncertainties of these parameters are a major sources of model errors. At the current stage, globally uniform values for model parameters are used as default which are tuned based on the sea ice state decades ago.

In this study, we attempted to estimate the mode state and parameter simultaneously using satellite and hydrographic observations in a coupled sea ice-ocean model. We extended the study of Lyu et al. (2023) by including the spatiotemporally varying model parameters in the control variables and optimized them together with the atmospheric forcing and the model initial conditions by assimilating large scale observations.

By assimilating satellite-measured SIC, SIT, SIV, along-track SLA, SST, and in-situ temperature and salinity profiles in 2012, the year with the recorded low summer Arctic extent, we explored the added effects of simultaneously state and parameter estimation (opti-SPE) over the tradiational state estimation (opti-SE). opti-SPE further reduces the cost function by 10.5%, especially for the SIC. In the control run and opti-SE, we note that the sea ice grows much slower over the open water in the Pacific sector during October, resulting in large negative SIC errors. By reducing the leads closing parameter Ho (orders of 0.1 m), opti-SPE acceralates the lateral sea ice growth in the open water. Since the sea ice cover impacts the heat flux from the ocean to the atmosphere heat flux significantly in Autumn, values of this parameter should be calibrated delicately for better simulating the ocean-sea ice-atmosphere interactions and quantifying the ocean and atmosphere heat fluxes.

Considering SIT, opti-SE and opti-SPE bring the simulated SIT within prior uncertainties of CS2SMOS data. Comparing with the independent ULS-measured SIT at the BGEP moorings, the two assimilation runs reproduce the seasonal sea ice evolution well. The differences of the assimilation run with respect to the ULS measurements are much smaller than that between CS2SMOS data and ULS measurements, especially from October to December. From the perspective of Lagrangian comparison, considering the sea ice evolutions along the six IMB trajectories, opti-SPE performs slightly better than opti-SE. Howevere, both the representativeness of IMB observations on local-scale ice thermodynamic processes and the contributions of sea ice dynamic deformation to ice thickening will affect the objective comparison between the simulation results and buoy measurements.

The overall improvements of data assimilation on sea ice velocities are not significant. In regions with compact ice, the two assimilation runs slightly improve the simulated sea ice velocity. However, as the buoys drifting into the marginal ice zone or the almost ice-free regions, the model simulations and the satellite may fail to simulate or monitor the small ice floes, resulting in large errors in sea ice velocities.

https://doi.org/10.5194/gmd-2024-189
Preprint. Discussion started: 30 April 2025

Despite that we use a relatively low-complex sea ice model as compared to the modern sea ice models such as the Los Alamos sea ice model (CICE; Hunke et al., 2020), the assimilation results demonstrate that the model simulations are brought into consistent with the satellite observations efficiently, which is also close to independent observations. Zampieri et al. (2021) also demonstrated that the low-complex sea ice model can be optimized more efficiently and the overall performance after optimization is mostly in line with the complex CICE configuration. Therefore, the low-complex sea ice model remains a suitable tools to for Arctic ocean and sea ice assimilation studies at the current stage. Indeed, we will update the sea ice module with the more complex CICE model in the next state and reconstruct the Arctic Ocean and sea ice changes using SPE.

Competing interests

The contact author has declared that none of the authors has any competing interests.

Acknowledgments

This research has been supported by the National Natural Science Foundation of China (grant No. 42325604), the National Key Research and Development Program of China (grant No. 2021YFC2803304), Program of Shanghai Academic/Technology Research Leader (Grant No. 22XD1403600), and the Southern Marine Science and Engineering Guangdong Laboratory (Zhuhai) (Grant No. ML2023SP219). For the assimilated sea ice variables, we thank the Alfred Wegener Institute, and EUMETSAT Ocean and Sea Ice Satellite Application Facility for supplying the CS2SMOS L4 sea ice thickness, OSI-SAF sea ice concentration and sea ice drift datasets, respectively. For the hydrographic observations, we acknowledge the Met Office, the Copernicus Marine Service, and the remoting sensing system for archiving and sharing the EN4, the along-track SLA, and sea surface temperature datasets. For the independent observations, we thank the Woods Hole Oceanographic Institution for the sea ice draft measured by the ULS， the Cold Regions Research and Engineering Laboratory-Dartmouth Mass Balance Buoy Program for the IMB data, the University of Washiongton for the buoy drifting trajectories.

Author contribution

Conceptualization: GL, AK, and LM. Experiments design and results analysis: GL. Investigation: RL, XL, and CL.

Original draft: GL. Review and editing: GL, LM, AK, RL, XL, and CL.

Open Research

Code and Data Availability Statement

The sea ice-ocean coupled model is based on MITgcm_c63m（https://mitgcm.org/download/other_checkpoints/). The modified MITgcm (c63m) codes are available to the public on Zenodo at https://doi.org/10.5281/zenodo.14584929 (Lyu et al., 2025). The sea ice variables and model parameters from the control run and the two assimilation runs are

https://doi.org/10.5194/gmd-2024-189
Preprint. Discussion started: 30 April 2025

Geoscientific Model Development Discussions
Open Access

available on Zenodo at https://doi.org/10.5281/zenodo.14584780 (Lyu, 2025). We note that a commercial TAF license is required to fully reproduce the optimization steps described in this study.

All the assimilated and independent validation are publicly available. The following datasets were provided with DOI numbers: the global ocean along track L3 sea surface heights can be downloaded from the E.U. Copernicus Marine Service Information (https://doi.org/10.48670/moi-00146); the sea ice concentration and drift data were based on the EUMETSAT OSI-450-a (doi:10.15770/EUM_SAF_OSI_0013), and osi-405-c (doi:10.15770/EUM_SAF_OSI_NRT_2007); the CryoSat-SMOS merged sea ice thickness data (https://doi.org/10.57780/sm1-4f787c3, European Space Agency., 2023) is available at https://spaces.awi.de/display/CS2SMOS/CryoSat-SMOS+Merged+Sea+Ice+Thickness.

The following datasets don't have DOI numbers, we provide their accessable links: the sea surface temperature were retrived from https://data.remss.com/SST/daily/mw_ir/v05.1/netcdf/ (last access: 13 April 2025, Gentemann et al., 1994); the EN.4.2.2 data were obtained from https://www.metoffice.gov.uk/hadobs/en4/ (last access: 13 April 2025, Good et al., 2013) and are ©British Crown Copyright, Met Office, 2013, provided under a Non-Commercial Government Licence http://www.nationalarchives.gov.uk/doc/non-commercial-government-licence/version/2/ (last access: 13 April 2025); the WOA18 climatological temperature and salinity data were download form https://www.ncei.noaa.gov/access/world-ocean-atlas-2018/ (last access, 13 April 2025, Locarnini et al., 2018; Zweng et al., 2018); the ULS-measured ice drafts were collected and shared by the Beaufort Gyre Exploration Program based at the Woods Hole Oceanographic Institution (https://www2.whoi.edu/site/beaufortgyre/data/mooring-data/, last access: 13 April 2025) in collaboration with researchers from Fisheries and Oceans Canada at the Institute of Ocean Sciences; the IMB-measured sea ice thickness were from http://imb-crrel-dartmouth.org/results/ (Perovich et al., 2025, last access: 13 April 2025); the sea ice drift trajecties were collected by the International Arctic Buoy Programme at https://iabp.apl.uw.edu/data.html (last access: 13 April 2025).

References

Annan, J. D., Hargreaves, J. C., Edwards, N. R., & Marsh, R. (2005). Parameter estimation in an intermediate complexity earth system model using an ensemble Kalman filter. *Ocean Modelling*, *8*(1), 135-154. https://doi.org/https://doi.org/10.1016/j.ocemod.2003.12.004

Branstator, G., & Teng, H. (2010). Two Limits of Initial-Value Decadal Predictability in a CGCM. *Journal of Climate*, *23*(23), 6292-6311. https://doi.org/https://doi.org/10.1175/2010JCLI3678.1

Bretherton, C. S., Henn, B., Kwa, A., Brenowitz, N. D., Watt-Meyer, O., McGibbon, J., Perkins, W. A., Clark, S. K., & Harris, L. (2022). Correcting Coarse-Grid Weather and Climate Models by Machine Learning From Global Storm-Resolving Simulations. *Journal of Advances in Modeling Earth Systems*, *14*(2), e2021MS002794. https://doi.org/https://doi.org/10.1029/2021MS002794

Chen, Y., Lei, R., Zhao, X., Wu, S., Liu, Y., Fan, P., Ji, Q., Zhang, P., & Pang, X. (2023). A new sea ice concentration product in the polar regions derived from the FengYun-3 MWRI sensors. *Earth Syst. Sci. Data*, *15*(7), 3223-3242. https://doi.org/10.5194/essd-15-3223-2023

European Space Agency, 2023, SMOS-CryoSat L4 Sea Ice Thickness, Version 206. https://doi.org/10.57780/sm1-4f787c3

Forget, G., Campin, J.-M., Heimbach, P., Hill, C. N., Ponte, R. M., and Wunsch, C. (2015). ECCO version 4: an integrated framework for non-linear inverse modeling and global ocean state estimation, *Geosci. Model Dev.*, 8, 3071–3104, https://doi.org/10.5194/gmd-8-3071-2015.

Fenty, I., & Heimbach, P. (2013). Coupled Sea Ice–Ocean-State Estimation in the Labrador Sea and Baffin Bay. *Journal of Physical Oceanography*, *43*(5), 884-904. https://doi.org/https://doi.org/10.1175/JPO-D-12-065.1

Fenty, I., Menemenlis, D., & Zhang, H. (2017). Global coupled sea ice-ocean state estimation. *Climate Dynamics*, *49*(3), 931-956. https://doi.org/10.1007/s00382-015-2796-6

Gentemann, C. L., Wentz, F. J., Mears, C. A., & Smith, D. K. (2004). In situ validation of Tropical Rainfall Measuring Mission microwave sea surface temperatures. *Journal of Geophysical Research: Oceans*, *109*(C4). https://doi.org/https://doi.org/10.1029/2003JC002092

Giering, R., & Kaminski, T. (1998). Recipes for adjoint code construction. *ACM Transactions on Mathematical Software (TOMS)*, *24*(4), 437-474.

Gilbert, J. C., & Lemaréchal, C. (2006). The module M1QN3.

Good, S. A., Martin, M. J., & Rayner, N. A. (2013). EN4: Quality controlled ocean temperature and salinity profiles and monthly objective analyses with uncertainty estimates. *Journal of Geophysical Research: Oceans*, *118*(12), 6704-6716. https://doi.org/10.1002/2013jc009067

Heimbach, P., Menemenlis, D., Losch, M., Campin, J.-M., & Hill, C. (2010). On the formulation of sea-ice models. Part 2: Lessons from multi-year adjoint sea-ice export sensitivities through the Canadian Arctic Archipelago. *Ocean Modelling*, *33*(1), 145-158. https://doi.org/https://doi.org/10.1016/j.ocemod.2010.02.002

Hibler, W. (1979). A Dynamic Thermodynamic Sea Ice Model. *Journal of Physical Oceanography*, *9*(4), 815-846. https://doi.org/10.1175/1520-0485(1979)009<0815:adtsim>2.0.co;2

Hibler , W. (1980). Modeling a Variable Thickness Sea Ice Cover. *Monthly Weather Review*, *108*(12), 1943-1973. https://doi.org/10.1175/1520-0493(1980)108<1943:mavtsi>2.0.co;2

Horvat, C., & Roach, L. A. (2022). WIFF1.0: a hybrid machine-learning-based parameterization of wave-induced sea ice floe fracture. *Geosci. Model Dev.*, *15*(2), 803-814. https://doi.org/10.5194/gmd-15-803-2022

Hourdin, F., Mauritsen, T., Gettelman, A., Golaz, J.-C., Balaji, V., Duan, Q., Folini, D., Ji, D., Klocke, D., Qian, Y., Rauser, F., Rio, C., Tomassini, L., Watanabe, M., & Williamson, D. (2017). The Art and Science of Climate Model Tuning. *Bulletin of the American meteorological Society*, *98*(3), 589-602. https://doi.org/https://doi.org/10.1175/BAMS-D-15-00135.1

Hu, X.-M., Zhang, F., & Nielsen-Gammon, J. W. (2010). Ensemble-based simultaneous state and parameter estimation for treatment of mesoscale model error: A real-data study. *Geophysical Research Letters*, *37*(8). https://doi.org/https://doi.org/10.1029/2010GL043017

Hunke, E. C., Allard, R., Bailey, D. A., Blain, P., Craig, A., Dupont, F., & Winton, M. (2020a). CICE-Consortium/CICE: CICE version 6.1.2 (version 6.1.2). Zenodo. https://doi.org/10.5281/zenodo.3888653

Jackson, C. S., Sen, M. K., Huerta, G., Deng, Y., & Bowman, K. P. (2008). Error Reduction and Convergence in Climate Prediction. *Journal of Climate*, *21*(24), 6698-6709. https://doi.org/https://doi.org/10.1175/2008JCLI2112.1

Kim, J. G., Hunke, E. C., & Lipscomb, W. H. (2006). Sensitivity analysis and parameter tuning scheme for global sea-ice modeling. *Ocean Modelling*, *14*(1), 61-80. https://doi.org/https://doi.org/10.1016/j.ocemod.2006.03.003

Kochkov, D., Yuval, J., Langmore, I., Norgaard, P., Smith, J., Mooers, G., Klöwer, M., Lottes, J., Rasp, S., Düben, P., Hatfield, S., Battaglia, P., Sanchez-Gonzalez, A., Willson, M., Brenner, M. P., & Hoyer, S. (2024). Neural general circulation models for weather and climate. *Nature*, *632*(8027), 1060-1066. https://doi.org/10.1038/s41586-024-07744-y

Koldunov, N. V., Köhl, A., Serra, N., & Stammer, D. (2017). Sea ice assimilation into a coupled ocean–sea ice model using its adjoint. *The Cryosphere*, *11*(5), 2265-2281. https://doi.org/10.5194/tc-11-2265-2017

Koo, Y., Lei, R., Cheng, Y., Cheng, B., Xie, H., Hoppmann, M., Kurtz, N. T., Ackley, S. F., & Mestas-Nuñez, A. M. (2021). Estimation of thermodynamic and dynamic contributions to sea ice growth in the Central Arctic using ICESat-2 and MOSAiC SIMBA buoy data. *Remote Sensing of Environment*, *267*, 112730. https://doi.org/https://doi.org/10.1016/j.rse.2021.112730

Krishfield, R. A., Proshutinsky, A., Tateyama, K., Williams, W. J., Carmack, E. C., McLaughlin, F. A., & Timmermans, M.-L. (2014). Deterioration of perennial sea ice in the Beaufort Gyre from 2003 to 2012 and its impact on the oceanic freshwater cycle. *Journal of Geophysical Research: Oceans*, *119*(2), 1271-1305. https://doi.org/https://doi.org/10.1002/2013JC008999

Lavergne, T., Eastwood, S., Teffah, Z., Schyberg, H., & Breivik, L.-A. (2010). Sea ice motion from low-resolution satellite sensors: An alternative method and its validation in the Arctic. *Journal of Geophysical Research: Oceans*, *115*(C10). https://doi.org/https://doi.org/10.1029/2009JC005958

Lavergne, T., Sørensen, A. M., Kern, S., Tonboe, R., Notz, D., Aaboe, S., Bell, L., Dybkjær, G., Eastwood, S., Gabarro, C., Heygster, G., Killie, M. A., Brandt Kreiner, M., Lavelle, J., Saldo, R., Sandven, S., & Pedersen, L. T. (2019). Version 2 of the EUMETSAT OSI SAF and ESA CCI sea-ice concentration climate data records. *The Cryosphere*, *13*(1), 49-78. https://doi.org/10.5194/tc-13-49-2019

Lei, R., Cheng, B., Hoppmann, M., Zhang, F., Zuo, G., Hutchings, J. K., Lin, L., Lan, M., Wang, H., Regnery, J., Krumpen, T., Haapala, J., Rabe, B., Perovich, D. K., & Nicolaus, M. (2022). Seasonality and timing of sea ice mass balance and heat fluxes in the Arctic transpolar drift during 2019–2020. *Elementa: Science of the Anthropocene*, *10*(1). https://doi.org/10.1525/elementa.2021.000089

Li, Z., Chao, Y., McWilliams, J. C., & Ide, K. (2008). A Three-Dimensional Variational Data Assimilation Scheme for the Regional Ocean Modeling System. *Journal of Atmospheric and Oceanic Technology*, *25*(11), 2074-2090. https://doi.org/https://doi.org/10.1175/2008JTECHO594.1

Lindsay, R. W., & Zhang, J. (2006). Assimilation of Ice Concentration in an Ice–Ocean Model. *Journal of Atmospheric and Oceanic Technology*, *23*(5), 742-749. https://doi.org/10.1175/jtech1871.1

Liu, C., Köhl, A., & Stammer, D. (2012). Adjoint-Based Estimation of Eddy-Induced Tracer Mixing Parameters in the Global Ocean. *Journal of Physical Oceanography*, *42*(7), 1186-1206. https://doi.org/10.1175/jpo-d-11-0162.1

Locarnini, R. A., Mishonov, A. V., Baranova, O. K., Boyer, T. P., Zweng, M. M., Garcia, H. E., Reagan, J. R., Seidov, D., Weathers, K. W., Paver, C. R., & V, S. I. (2018). World Ocean Atlas 2018, Volume 1: Temperature. *Levitus, edited by: Mishonov, A., NOAA Atlas NESDIS*, *82*, 52.

Losch, M., Menemenlis, D., Campin, J.-M., Heimbach, P., & Hill, C. (2010). On the formulation of sea-ice models. Part 1: Effects of different solver implementations and parameterizations. *Ocean Modelling*, *33*(1), 129-144. https://doi.org/https://doi.org/10.1016/j.ocemod.2009.12.008

Lu, Y., Wang, X., & Dong, J. (2021). Melt Pond Scheme Parameter Estimation Using an Adjoint Model. *Advances in Atmospheric Sciences*, *38*(9), 1525-1536. https://doi.org/10.1007/s00376-021-0305-x

Lyu, G., Koehl, A., Serra, N., & Stammer, D. (2021a). Assessing the current and future Arctic Ocean observing system with observing system simulating experiments. *Quarterly Journal of the royal meteorological society*, *147*(738), 2670-2690. https://doi.org/https://doi.org/10.1002/qj.4044

Lyu, G., Koehl, A., Serra, N., Stammer, D., & Xie, J. (2021b). Arctic ocean–sea ice reanalysis for the period 2007–2016 using the adjoint method. *Quarterly Journal of the royal meteorological society*, *147*(736), 1908-1929. https://doi.org/https://doi.org/10.1002/qj.4002

Lyu, G., Koehl, A., Wu, X., Zhou, M., & Stammer, D. (2023). Effects of including the adjoint sea ice rheology on estimating Arctic Ocean–sea ice state. *Ocean Sci.*, *19*(2), 305-319. https://doi.org/10.5194/os-19-305-2023

Lyu, G., Köhl, A., Matei, I., & Stammer, D. (2018). Adjoint-Based Climate Model Tuning: Application to the Planet Simulator. *Journal of Advances in Modeling Earth Systems*, *10*(1), 207-222. https://doi.org/https://doi.org/10.1002/2017MS001194

Lyu, G . (2025). MITgcm model developed for state and parameter estimation in a pan-Arctic ocean and sea ice model. Zenodo. https://doi.org/10.5281/zenodo.14584929

Lyu, G ., Mu, L., Koehl, A., Lei, R., Liang, X., & Liu, C. (2025). MITgcm model developed for state and parameter estimation in a pan-Arctic ocean and sea ice model using MITgcm (c63m) [Data set]. Zenodo. https://doi.org/10.5281/zenodo.14584780

Marshall, J., Adcroft, A., Hill, C., Perelman, L., & Heisey, C. (1997). A finite‐volume, incompressible Navier Stokes model for studies of the ocean on parallel computers. *Journal of Geophysical Research: Oceans*, *102*(C3), 5753-5766.

Massonnet, F., Goosse, H., Fichefet, T., & Counillon, F. (2014). Calibration of sea ice dynamic parameters in an ocean-sea ice model using an ensemble Kalman filter. *Journal of Geophysical Research: Oceans*, *119*(7), 4168-4184. https://doi.org/https://doi.org/10.1002/2013JC009705

Mauritsen, T., Stevens, B., Roeckner, E., Crueger, T., Esch, M., Giorgetta, M., Haak, H., Jungclaus, J., Klocke, D., Matei, D., Mikolajewicz, U., Notz, D., Pincus, R., Schmidt, H., & Tomassini, L. (2012). Tuning the climate of a global model. *Journal of Advances in Modeling Earth Systems*, *4*(3). https://doi.org/https://doi.org/10.1029/2012MS000154

Miller, P. A., Laxon, S. W., & Feltham, D. L. (2005). Improving the spatial distribution of modeled Arctic sea ice thickness. *Geophysical Research Letters*, *32*(18). https://doi.org/https://doi.org/10.1029/2005GL023622

Mu, L., Losch, M., Yang, Q., Ricker, R., Losa, S. N., & Nerger, L. (2018). Arctic-Wide Sea Ice Thickness Estimates From Combining Satellite Remote Sensing Data and a Dynamic Ice-Ocean Model with Data Assimilation During the CryoSat-2 Period. *Journal of Geophysical Research: Oceans*, *123*(11), 7763-7780. https://doi.org/https://doi.org/10.1029/2018JC014316

Murphy, J. M., Sexton, D. M. H., Barnett, D. N., Jones, G. S., Webb, M. J., Collins, M., & Stainforth, D. A. (2004). Quantification of modelling uncertainties in a large ensemble of climate change simulations. *Nature*, *430*(7001), 768-772. https://doi.org/10.1038/nature02771

Nguyen, A. T., Menemenlis, D., & Kwok, R. (2011). Arctic ice-ocean simulation with optimized model parameters: Approach and assessment. *Journal of Geophysical Research: Oceans*, *116*(C4). https://doi.org/https://doi.org/10.1029/2010JC006573

Nguyen, A. T., Pillar, H., Ocaña, V., Bigdeli, A., Smith, T. A., & Heimbach, P. (2021). The Arctic Subpolar Gyre sTate Estimate: Description and Assessment of a Data-Constrained, Dynamically Consistent Ocean-Sea Ice Estimate for 2002–2017. *Journal of Advances in Modeling Earth Systems*, *13*(5), e2020MS002398. https://doi.org/https://doi.org/10.1029/2020MS002398

Panteleev, G., Yaremchuk, M., Stroh, J. N., Francis, O. P., & Allard, R. (2020). Parameter optimization in sea ice models with elastic–viscoplastic rheology. *The Cryosphere*, *14*(12), 4427-4451. https://doi.org/10.5194/tc-14-4427-2020

Perovich, D., J. Richter-Menge, and C. Polashenski, Observing and understanding climate change: Monitoring the mass balance, motion, and thickness of Arctic sea ice, http://imb-crrel-dartmouth.org , 2025.

Pujol, M. I., Faugère, Y., Taburet, G., Dupuy, S., Pelloquin, C., Ablain, M., & Picot, N. (2016). DUACS DT2014: the new multi-mission altimeter data set reprocessed over 20 years. *Ocean Sci.*, *12*(5), 1067-1090. https://doi.org/10.5194/os-12-1067-2016

Richter-Menge, J. A., Perovich, D. K., Elder, B. C., Claffey, K., Rigor, I., & Ortmeyer, M. (2006). Ice mass-balance buoys: a tool for measuring and attributing changes in the thickness of the Arctic sea-ice cover. *Annals of Glaciology*, *44*, 205-210. https://doi.org/10.3189/172756406781811727

Ricker, R., Hendricks, S., Kaleschke, L., Tian-Kunze, X., King, J., & Haas, C. (2017). A weekly Arctic sea-ice thickness data record from merged CryoSat-2 and SMOS satellite data. *The Cryosphere*, *11*(4), 1607-1623. https://doi.org/10.5194/tc-11-1607-2017

Sumata, H., Kauker, F., Karcher, M., & Gerdes, R. (2019). Simultaneous Parameter Optimization of an Arctic Sea Ice–Ocean Model by a Genetic Algorithm. *Monthly Weather Review*, *147*(6), 1899-1926. https://doi.org/10.1175/mwr-d-18-0360.1

Taburet, G., Sanchez-Roman, A., Ballarotta, M., Pujol, M. I., Legeais, J. F., Fournier, F., Faugere, Y., & Dibarboure, G. (2019). DUACS DT2018: 25 years of reprocessed sea level altimetry products. *Ocean Sci.*, *15*(5), 1207-1224. https://doi.org/10.5194/os-15-1207-2019

Taylor, K. E. (2001). Summarizing multiple aspects of model performance in a single diagram. *Journal of Geophysical Research: Atmospheres*, *106*(D7), 7183-7192.

Uotila, P., O'Farrell, S., Marsland, S. J., & Bi, D. (2012). A sea-ice sensitivity study with a global ocean-ice model. *Ocean Modelling*, *51*, 1-18. https://doi.org/https://doi.org/10.1016/j.ocemod.2012.04.002

https://doi.org/10.5194/gmd-2024-189
Preprint. Discussion started: 30 April 2025

von Albedyll, L., Hendricks, S., Grodofzig, R., Krumpen, T., Arndt, S., Belter, H. J., Birnbaum, G., Cheng, B., Hoppmann, M., Hutchings, J., Itkin, P., Lei, R., Nicolaus, M., Ricker, R., Rohde, J., Suhrhoff, M., Timofeeva, A., Watkins, D., Webster, M., & Haas, C. (2022). Thermodynamic and dynamic contributions to seasonal Arctic sea ice thickness distributions from airborne observations. *Elementa: Science of the Anthropocene*, *10*(1). https://doi.org/10.1525/elementa.2021.00074

Weaver, A. T., & Mirouze, I. (2013). On the diffusion equation and its application to isotropic and anisotropic correlation modelling in variational assimilation. *Quarterly Journal of the Royal Meteorological Society*, *139*(670), 242-260. https://doi.org/https://doi.org/10.1002/qj.1955

Williamson, D., Goldstein, M., Allison, L., Blaker, A., Challenor, P., Jackson, L., & Yamazaki, K. (2013). History matching for exploring and reducing climate model parameter space using observations and a large perturbed physics ensemble. *Climate Dynamics*, *41*(7), 1703-1729. https://doi.org/10.1007/s00382-013-1896-4

Wu, X., Zhang, S., Liu, Z., Rosati, A., Delworth, T. L., & Liu, Y. (2012). Impact of Geographic-Dependent Parameter Optimization on Climate Estimation and Prediction: Simulation with an Intermediate Coupled Model. *Monthly Weather Review*, *140*(12), 3956-3971. https://doi.org/https://doi.org/10.1175/MWR-D-11-00298.1

Yang, B., Qian, Y., Lin, G., Leung, L. R., Rasch, P. J., Zhang, G. J., McFarlane, S. A., Zhao, C., Zhang, Y., Wang, H., Wang, M., & Liu, X. (2013). Uncertainty quantification and parameter tuning in the CAM5 Zhang-McFarlane convection scheme and impact of improved convection on the global circulation and climate. *Journal of Geophysical Research: Atmospheres*, *118*(2), 395-415. https://doi.org/https://doi.org/10.1029/2012JD018213

Zampieri, L., Kauker, F., Fröhle, J., Sumata, H., Hunke, E. C., & Goessling, H. F. (2021). Impact of Sea-Ice Model Complexity on the Performance of an Unstructured-Mesh Sea-Ice/Ocean Model under Different Atmospheric Forcings. *Journal of Advances in Modeling Earth Systems*, *13*(5), e2020MS002438. https://doi.org/https://doi.org/10.1029/2020MS002438

Zhang, F., Pang, X., Lei, R., Zhai, M., Zhao, X., & Cai, Q. (2022). Arctic sea ice motion change and response to atmospheric forcing between 1979 and 2019. *International Journal of Climatology*, *42*(3), 1854-1876. https://doi.org/https://doi.org/10.1002/joc.7340

Zhang, J., & Hibler , W. (1997). On an efficient numerical method for modeling sea ice dynamics. *Journal of Geophysical Research: Oceans*, *102*(C4), 8691-8702.

Zhang, S. (2011). A Study of Impacts of Coupled Model Initial Shocks and State–Parameter Optimization on Climate Predictions Using a Simple Pycnocline Prediction Model. *Journal of Climate*, *24*(23), 6210-6226. https://doi.org/https://doi.org/10.1175/JCLI-D-10-05003.1

Zweng, M. M., Reagan, J. R., Seidov, D., Boyer, T. P., Locarnini, R. A., Garcia, H. E., Mishonov, A. V., Baranova, O. K., Weathers, K. W., Paver, C. R., & V, S. I. (2018). World Ocean Atlas 2018, Volume 2: Salinity. *Levitus, edited by: Mishonov, A., NOAA Atlas NESDIS*, *82*, 50.